Influence of Alloy Solidification Path on Melt Pool Behavior in Additive Manufacturing

S. Wells[1,2], A. Plotkowski[3], J. Coleman[4], M. J. M. Krane[1]

[1]Purdue Center of Metal Casting Research; School of Materials Engineering, Purdue University, West Lafayette, IN

[2]Currently: Department of Mechanical Engineering, Colorado School of Mines, Golden, CO

[3]Materials Science and Technology Division, Oak Ridge National Laboratory, Oak Ridge, TN

[4]Computational Sciences & Engineering Division, Oak Ridge National Laboratory, Oak Ridge, TN

Abstract

Numerical models used to study transport phenomena in laser-powder bed fusion processes often rely on assumptions and simplifications to reduce their computational expense. One common simplification is in the description of latent heat evolution during the solid-liquid phase change (*i.e.,* the solidification pathway), justified by the fact that the mushy zone thickness is similar to the numerical grid spacing used for continuum transport models. The lack of resolution of transport phenomena in the mushy zone motivates the use of computationally convenient solidification paths such as linear or sigmoidal relationships over pathways derived from fundamental solidification theory such as equilibrium or Scheil models. In the present work, an uncertainty quantification (UQ) framework is used to analyze the influence of solidification pathway selection on the solidification dynamics and melt pool geometries in laser based additive manufacturing (AM) of IN625. Results show the solidification pathway has a quantifiable influence on the cooling rate at the liquidus isotherm, mushy zone thickness, and solidification time. Due to similarities in the latent heat evolution at the beginning of solidification, the equilibrium and Scheil models predict

similar cooling rates near the liquidus isotherm, however the wider freezing range of Scheil leads to a wider mushy zone compared to equilibrium. The non-physical latent heat release profiles of sigmoidal and linear paths lead to significant overpredictions of undercooling at the liquidus isotherm compared to equilibrium and Scheil. These results indicate that careful consideration should be given to the choice of solidification pathway to ensure reliable model predictions.

1. Introduction

Laser powder bed fusion (L-PBF) is a state-of-the-art manufacturing method whereby a thin layer of metal powder particles is melted by a laser heat source at a fine scale (100-200 microns) under an inert atmosphere, a process which is repeated over many subsequent layers. This layer-by-layer process features several advantages over traditional casting and wrought-based methods such as a reduction of parts necessary for an assembly [1]. Additionally, the small size of the melt pool allows for near-net, difficult to cast, shapes to be produced, thereby reducing the need for post-process machining [2]. Alloy systems demonstrated to be suitable for the L-PBF process include Ti-6Al-4V, 316 stainless steel, and difficult to machine alloys such as Inconel 625 and 718, which, along with the previously discussed advantages, make this additive manufacturing process ideal for the biomedical, automotive, and aerospace industries [1].

Unfortunately, despite these advantages, inconsistent build quality and defect formation [3-5] have presented obstacles to certification of structural components produced by L-PBF and limited more widespread industrial adoption. As a result, the reduction and elimination of defects such as lack of fusion and keyholing are current topics of extensive ongoing research. Due to the restrictively high financial and temporal expense of experimental studies, numerical models are often used. These models can provide valuable insight into the processing conditions and scan strategies which contribute to detrimental defect formation [6] at the melt pool scale, anticipated microstructures at grain evolution scale [7-9], as well as the resulting anisotropic mechanical behavior via crystal plasticity modeling [10-12].

The capability of numerical models to simulate and make predictions for additive manufacturing is a vital step to improve our current understanding of the physics involved and the process-property relations. However, these models often leverage simplifications as tradeoffs between model fidelity and computational expense. Moges *et al.* [13] reviewed several numerical models of L-PBF and categorized model inaccuracies based on the simplifications made and the

model functionality in which the inaccuracy occurred. For melt pool scale simulations, the inaccuracy source taxonomy purposed by Moges *et al.* includes 1) powder bed, 2) heat source, 3) melt pool, and 4) solidification. Previous work [14] investigated the role of input parameter uncertainty on model predictions using an experimentally validated finite volume method (FVM) model; however, the investigated input parameters fall exclusively within the first three categories. The effect the chosen solid fraction-temperature relation has on melt pool shape and solidification dynamics was not considered.

Various possible solidification pathways relate the local solid fraction (f_s) to temperature in the range between the solidus and liquidus isotherms of an alloy, generally referred to as the '*mushy zone*' (illustrated in Figure 1). These relations, of the form $f_s(T)$, take different shapes (*e.g.*, linear, exponential, etc.) and so have different $\partial f_s/\partial T$ profiles. Because the latent heat release at any given temperature is proportional to $\partial f_s/\partial T$, the choice of the solidification path governs the distribution of latent heat release over the alloy freezing range. Often in AM modeling, the $f_s(T)$ is chosen for simplicity (*e.g.*, a linear function) or faster convergence (*e.g.*, a sigmoidal function), rather than physical fidelity. Justification for this simplification is the extreme cooling rates and thermal gradients observed within the melt pool. Hooper [15] reported cooling rates in excess of 10^6 K/s with thermal gradients between 4-20 K/μm, which agree with the observations of the present numerical model. Under such conditions, it is often assumed the mushy-zone thicknesses for melt pool scale simulations would be on the same length scale as the mesh size, leading to insufficient spatial resolution of the mushy zone and thus the latent heat release profile. Despite this, the above thermal gradients would predict mushy zone thicknesses greater than 50 microns for IN625 (assuming non-equilibrium solidification with a freezing range of 210K). As such, it is assumed that because the mushy zone is not adequately resolved, a $f_s(T)$ which does not closely match reality can be used without significant effect on model predicts as long as the model accounts for all the latent heat.

Using this assumption, a variety of $f_s(T)$ functions have been applied by models of AM. Four such solidification paths include: 1) equilibrium (lever-rule), 2) Scheil, 3) linear [16-18], and 4) sigmoidal [14,19,20]. These four functions are shown in Figure 2 for Inconel 625, the alloy of interest in the present work. As the name implies, equilibrium assumes thermodynamic equilibrium in both the solid and liquid phases of the alloy, as solute diffusion in both phases is

assumed to be significantly faster than the solidification front velocity. Due to the high cooling rates in the AM process, non-equilibrium microsegregation is observed in many alloy systems, including IN625, thus $f_s(T)$ may be better represented by the Scheil thermodynamic model. The Scheil model assumes diffusion occurs infinitely fast in the liquid phase, but not at all in the solid. The freezing range predicted by the equilibrium model is smaller than that of Scheil, as the latter lowers the solidus temperature to a terminal eutectic reaction. In addition to these two physics-based relations, the linear approximation [16-18] has been used due to the ease of implementation. A sigmoidal function [14,19,20] has also been used as it is continuous and differentiable with temperature over the entire freezing range, enabling an implicit form of the transient latent heat term which could converge with fewer iterations.

The purpose of the present work is to evaluate how the different solidification pathways influence the melt pool geometries (maximum width, depth, and length calculated by the solidus isotherm) and solidification dynamics (cooling rate at the liquidus isotherm, solidification time, and mushy-zone thickness) in an experimentally calibrated FVM melt pool transport model. By directly comparing model behavior for the four solidification pathways, we can evaluate the assumption that model predictions are insensitive to the choice of solidification pathway and associated latent heat release profiles due to insufficient resolution of the mushy zone. The outputs of interest were selected because melt pool geometry is used for scan strategy development, cooling rate at the liquidus isotherm and solidification time can be used as an input for microstructure evolution models, and mushy-zone thickness is a simple metric which can be easily visualized and compared between the pathways. The UQ framework developed in previous work [14] is applied here to quantify the sensitivity of model predictions to the choice in $f_s(T)$, and in doing so, we can quantify how this assumption impacts the confidence that a numerical model accurately represents the reality it is supposed to simulate, referred to here simply as 'model reliability'.

2. Methodology

To determine the effect of solidification path on model prediction and uncertainty, a similar analysis method described in [14] was used. This method uses an experimentally calibrated finite volume L-PBF model based in OpenFOAM [20] to predict the transport phenomenon and solidification behavior of the melt pool. This code is coupled with TASMANIAN [21-25], to

generate polynomial surrogate models for the model predictions of interest. The surrogate models are sampled by a Monte Carlo (MC) based technique to generate probability density functions (PDFs) for the outputs of interest.

2.1 Melt Pool Transport Model

A finite volume method transport model based in OpenFOAM [20] was used to simulate the L-PBF process as detailed by Coleman *et al.* [20]. The model was previously validated by comparing melt pool predictions to the work by Heigel and Lane [26], and Ghosh [27]. The present analysis is restricted to processing conditions in the conduction dominant regime, *i.e.,* high scan speeds and low laser powers, so that the calculation of fluid flow in the melt pool may be reasonably neglected. Under these conditions, the conservation of energy in terms of temperature for a continuum solid-liquid mixture is:

$$\rho c_p \frac{\partial T}{\partial t} = \nabla \cdot (k \nabla \mathrm{T}) + \rho L_f \frac{\partial f_s}{\partial t} + \dot{Q} \tag{1}$$

where ρ is density, c_p is specific heat, T is temperature, t is time, k is thermal conductivity, L_f is latent heat of fusion, f_s is the solid mass fraction, and $\dot{Q}$ is the volumetric heat source. The density and specific heat are taken as constant values at the liquidus temperature, whereas the thermal conductivity is temperature dependent. The second to last term represents the latent heat evolution during the solid-liquid phase change, where the solid mass fraction is specified in terms of the local temperature. The different solidification pathways investigated in this work are shown in Figure 2. The last term represents the power density distribution due to the moving heat source and is treated as a Gaussian [28], such that:

$$\dot{Q} = \frac{2\eta P}{r^2 d\left(\pi/3\right)^{3/2}} exp\left(-3\left[\frac{((x - x_b) + y)^2}{r^2} + \frac{z^2}{d^2}\right]\right) \tag{2}$$

where η is absorption, r is the radius, and d is the penetration of the laser heat source. The scan direction is along the x-axis, where x_b is the starting location for the laser scan, and z is the depth into the part from the top surface. As detailed by Coleman *et al.* [20], the value for laser absorption is not based on experimental absorptivity measurements, rather it is calibrated by matching the predicted isotherms to known melt pool dimensions [26,27]. The radius of the laser heat source is

assumed to be a constant value of 85.7 μm and the baseline penetration depth is given a value of 20 μm.

The property data for Inconel 625 used in the present study originated from work by Coleman *et al.* [20]. These values are summarized in Table 1.

2.1.1 Mesh and Time Step

The current calculations only consider a single line scan, with a domain size of 5.0 x 0.8 x 0.4 mm (x, y, z) shown in Figure 3.

A convergence study in [20] found a grid-converged solution for the model used here was reached with a cell spacing of 12.5 μm in x, and 6.25 μm in y and z. Given that the present work is evaluating how well the mushy zone and latent heat release profiles are resolved, baseline simulations for each of the solidification paths were executed at various spatial resolutions to identify if a grid independent solution could be reached. Figure 4 illustrates that even at very fine grid spacing (5 μm), clear convergence is not satisfied. Mushy zone thickness (calculated by multiplying scan speed V_{scan} with solidification time t_s) was used here as a generic descriptor of the mushy zone that was of similar magnitude for all solidification paths. While a grid independent solution may (or may not) occur on an even finer grid, the resolution needed would be prohibitively expensive computationally. We have elected to use a 5 μm grid to maintain computational affordability while minimizing the resulting numerical error. Interestingly, the linear and sigmoidal curves seem closer to a converged solution at the cutoff grid size due to their smaller latent heat release profile at the onset of solidification, i.e., the latent heat release profiles near the liquidus isotherm are less sensitive to error caused by insufficient spatial resolution for linear and sigmoidal. In [14] a timestep of 1 μs was used to ensure sufficient temporal resolution; however, the assumption that the solidification pathway was not adequately resolved in space was also used. One purpose of the current work is to investigate the validity of this assumption and what effect it may have on the uncertainty of model predictions. As such, a timestep of 0.1 μs was used to maximize temporal resolution and ensure the spatial resolution of the grid is the limiting factor in resolving the mushy zone and latent heat release profile.

Model predictions of melt pool geometry (length, width, and depth), cooling rate, solidification time, and mushy zone thickness were recorded once a steady-state condition was met. This

condition is established at a location where the melt pool shape is no longer a function of distance from the scan starting point. The solidification time was probed and calculated by tracking the time when the liquid fraction for the given cell drops below 1.0 until reaching a value of 0.001 liquid. Cooling rates are recorded at the liquidus isotherm, and mushy zone thickness is calculated by multiplying the solidification time by the laser scan speed. Solidification time, cooling rate, and mushy zone thickness were all calculated along the top surface through the middle of the melt pool along the scan direction. Baseline measurements for the melt pool geometries, cooling rates, solidification times, and mushy zone thickness for each of the solid fraction-temperature relations are listed in Table 3.

2.2 Uncertainty Analysis

For the present work, an uncertainty quantification framework [14] was employed to evaluate the influence of solidification path selection on the uncertainty in model predictions. The non-intrusive library TASMANIAN [21-25] was used to generate sparse grids for each of the solid fraction-temperature relations, and a polynomial surrogate model was fit to the model predictions (responses) corresponding to the sparse grid abscissas. The polynomial surrogate models are fed a limited number of input parameter values (corresponding to the inputs parameters used in its construction) and produce approximations for each of the outputs of interest that closely match the predictions of the full-scale numerical model, but at a fraction of the time needed to solve. Probability density functions for the outputs of interest were produced by sampling each of the surrogate models via a Monte Carlo based method. These probability distributions represent the uncertainty in each of the model predictions, an easy metric to compare the solidification pathway models and evaluate their influence on the physics involved in the L-PBF model.

2.2.1 Sensitivity Analysis

Table 2 contains 13 input parameters for the numerical model along with estimates of their respective uncertainties. Previous work [14], demonstrated that the number of uncertain input parameters could be down selected by only account for the 3 most sensitive input parameters (referred to as the reduced order analysis) and still capture nearly all the uncertainty in our model predictions. For the sparse grid used here, the number of simulations needed to construct a surrogate goes as $2n^2 + 1$ where n corresponds to the number of input parameters. By reducing the dimensionality of our parameter space, the upfront cost of constructing the surrogate models

was reduced. Sensitivity analysis was conducted for each of the solidification paths individually. Trends and relative sensitivities were found to match those of [14] for all four paths, thus the reduced order analysis is valid for the present work.

2.2.2 Surrogate Model Construction and Validation

From the sensitivity analysis, a sparse grid for each pathway was generated where grid level corresponds to the order of analysis (the number of points on the grid). Each point on the sparse grid corresponds to a set of input values for the numerical model. Results from the numerical model at each of these points is fed back to TASMANIAN as a response. Interpolation between responses was then modeled using a summation of Lagrangian polynomials to construct a response surface which acts as the surrogate model. One surrogate model is produced for each of the outputs of interest. Each surrogate model was validated by sampling with input parameter sets off the sparse grid points (where interpolation error is expected to be highest) and comparing those results with evaluations of the full-scale numerical model under the same conditions. Good agreement at these validation points ensures the surrogate model predictions are reliable approximations of the AM transport model behavior throughout the parameter space.

2.2.3 Monte Carlo Sampling

The surrogate models were sampled by a Monte Carlo based method using 10 million random values to produce probability density functions (PDFs) for each of the outputs of interest, which as mentioned above, illustrate the uncertainty in the outputs of interest resulting from uncertainty in the input parameters (*i.e.,* the propagation of uncertainty through the model). The input parameters values used for sampling were selected from a Gaussian distribution centered at the mean values reported in Table 1.

3. Results

3.1 Baseline

Baseline simulations were run for each of the solidification path models with no consideration of uncertainty. Table 2 summarizes the model predictions under these conditions. The baseline values change depending on the solidification pathways, thus indicating that the assumption that the mushy zone is not adequately resolved to make a difference does not hold for the present

model. Specifically, melt pool width and depth calculations are consistent between the models except for equilibrium which predicts a smaller pool due to its lower freezing range and higher solidus temperature. The non-physical latent heat release curves (linear and sigmoidal) both predict much greater cooling rates at the liquidus isotherm, though interestingly, they still predict longer solidification times and thicker mushy zones.

3.2 Uncertainty Analysis

3.2.1 Surrogate Model Construction, Validation, and Sampling

The 'reduced order analysis' [14] is employed here to reduce the uncertain input parameter space to the laser absorptivity, solid and liquid specific heat capacities of Inconel 625. A level-2 sparse grid was generated in TASMANIAN featuring 19 points, corresponding to 19 numerical simulations (for each solidification path models) to construct the polynomial surrogate models. Each surrogate model was validated, and error was found to be 2% or lower for all outputs and solidification pathways.

By sampling each surrogate 10 million times over the ranges of input uncertainties, the probability distributions of each output of interest are established for each of the four solidification pathways. Figure 4 compares the PDFs for the different solidification pathway models for all outputs of interest. Here we observe that while the melt pool width and depth predictions for the Scheil, linear, and sigmoidal models show good agreement, both linear and sigmoidal predict larger values for cooling rate at the liquidus isotherm, solidification time at the top surface, and thickness of the mushy zone. The opposite is true for the equilibrium thermodynamic model which shows good agreement with Scheil for cooling rates at the liquidus isotherm, but smaller melt pools, solidification times, and mushy zone thickness. Table 3 presents the statistics from these PDFs. Comparing the PDF statistics, it was found that the uncertainty in the model predictions seems insensitive to the pathway used (*i.e.,* while the mean and standard deviation are affects by f_s (T), proportionality between them remains the same).

3.3 Sensitivity Analysis

The three input parameters which showed the highest sensitivity are the laser absorption efficiency, and solid and liquid specific heat capacity of the alloy, which matches results from

[14]. The absorption efficiency of the laser heat source was assigned a relatively high uncertainty (10% of the most likely value) for two reasons. Firstly, the laser absorption efficiency value used is not derived from experimental measurements of effective absorptivity but rather used to calibrate the transport model against experimental melt pool cross-sections. Second, laser absorptivity of powder bed systems is difficult to quantify. In addition to the fluctuating liquid surface of the molten pool, the laser may interact with powder ahead of the melt pool which would possess a greater effective absorptivity that bulk IN625 due to entrapment of the laser between powder particles. This parameter shows up in the volumetric heat source term which models the input of thermal energy, much the same as the laser power. However, the uncertainty in laser power (~2% of the most likely value) is much lower than absorption efficiency as more precise measurement and monitoring methods and devices exist in AM systems.

Solid and liquid specific heat capacities of IN625 were found to have the second and third highest sensitivities. These parameters directly affect the sensible heating and cooling during solidification. From a model standpoint, both parameters show up in the energy storage term (left-hand side of Eqn. 1) which mathematically describes the rate of change of sensible heat as a function of time. Similar to laser absorption efficiency and power, the specific heat capacity is multiplied by the alloy density in Eqn. 1, and like laser power, a lower sensitivity is observed for density due to its lower uncertainty.

3.4 Effect on Melt Pool Dimensions

From the PDFs presented in Figure 5 and distribution statics in Table 3, several observations can be made regarding melt pool dimensions. Firstly, choice in the solidification pathway model seems not to affect the predicted pool width and depth (except equilibrium due to the higher T_{solidus}). Second, the latent heat release profile has a strong influence on melt pool length.

Insensitivity of the melt pool width and depth can be attributed to the thicknesses of the mushy zone at these regions. Compared to the tail, the extreme thermal gradients at the sides and bottom of the melt pool result in mushy zones of only a few microns and faster conduction of latent heat away from the melt pool. In these regions, the assumption that the mushy zone is not adequately resolved to capture latent heat release profiles holds for the present model as a grid spacing much finer than the 5 microns used would be required. However, even if a sufficiently fine grid were used to capture the latent heat release in these regions of the melt pool, given that the thickness of

the mushy zone (<5μm), the effects of solidification pathway selection would fall within the uncertainty in the model predictions, which was found to be on the order of 1.5 μm and 2.5 μm for the width and depth respectively (given by Table 3). Resolving these regions of the melt pool's mushy zone would require a significant increase in computational load, but yield only minimal gain in model fidelity and model predictions which are no-less uncertain.

3.5 Mushy Zone Solidification Dynamics

Figure 5 and the statistics of Table 3 show that the cooling rate at the liquidus isotherm, solidification time, and mushy zone thickness are highly sensitive to the solidification pathway used. Immediately this indicates that through the melt pool tail (where the mushy zone is on the order of 100 μm) the release of latent heat, dictated by $f_s(T)$, can be adequately resolved to quantify its effect on the solidification dynamics which govern dendrite growth and microstructure development. As the mushy zone thicknesses differ for each pathway, direct comparisons of the solidification behavior are difficult without normalized data. To achieve this, we define a new relative position through the mushy zone $\mathrm{x_{rel}}$ defined by Eq. 8, which normalizes the position along the x-axis (x) through the mushy zone to a unit interval

$$\mathrm{x_{rel}} = \frac{\mathrm{x} - \mathrm{x_{fully\ solidified}}}{\mathrm{x_{liquidus}} - \mathrm{x_{fully\ solidified}}}, \tag{3}$$

where $\mathrm{x_{rel}} = 0$ occurs at the positions where the alloy has fully solidified (solidus isotherm for equilibrium, and eutectic temperature for all others), and $\mathrm{x_{rel}} = 1$ at the position of the liquidus isotherm illustrated by Figure 6.

By normalizing position, it is possible to plot and compare the temperature profiles $T(\mathrm{x_{rel}})$, and cooling rate profiles $CR(\mathrm{x_{rel}})$ through the mushy zone, given by Figure 7 and 8 respectively, to better understand the effect of each solidification pathway. Both the Scheil and equilibrium models release a significant fraction of their latent heat in the upper end of the freezing range (corresponding to a shallow slope in Figure 2) which tapers off at the lower end of the freezing range. The initial rapid release of latent heat acts to slow the rate of cooling which results in low cooling rates and a gradual decrease in temperature at and near the liquidus isotherm. Both effects are observed by the PDF statistics of Table 3 as well as Figures 8 and 9.

The sigmoidal curve predicts almost no latent heat release near both liquidus and solidus isotherms but at a consistent rate through the middle of the freezing range. This behavior results in steeper cooling rates near the liquidus and solidus temperatures with a lower rate through the middle of the freezing range (Figure 8). Lastly, linear consistently releases latent heat throughout the entire freezing range which produces a consistent cooling rate and subsequent temperature profile. Figures 8 and 9 match the expected behavior indicating the solidification pathways and latent heat release profiles are being captured.

Figures 8 and 9 clearly illustrate that the selection of solidification pathway influences the cooling rates and temperature profiles through the mushy zone. The Scheil and equilibrium thermodynamic models release the majority of their latent heat at temperatures near the liquidus isotherm. By expending all the latent heat early, conductive heat transfer quickly dissipates heat into the surrounding material resulting in very large cooling rates near the solidus, as observed on the left side of Figure 7. Equilibrium has the shortest solidification time as it not only suffers this early latent heat release, but also assumes a much narrower freezing range. The sigmoidal and linear curves release their latent heat much more gradually during solidification. Overall, this produces lower, but more consistent cooling rates throughout the mushy zone than Scheil as the latent heat is steadily being released to counteract the dissipation of heat to the surrounding material. These observations can be further supported by plotting the thermal gradient (G) vs the solidification front velocity (V). In Figure 9, we see a narrower range (fewer orders of magnitude) of G for the linear and sigmoidal curves which is indicative of the more consistent latent heat release and subsequent cooling rates. When comparing the solidification paths, we see a clear dependence at regions of the melt pool where the front velocity is high and the temperature gradient is low (melt pool tail), which is not observed elsewhere. By overlaying a Péclet number (defined as the ratio of advective to diffusive heat transfer) equal to one (as defined by Stump *et.al.* [29]) it is apparent that for regions of the melt pool which are diffusion (conduction) controlled ($Pé < 1$), the solidification pathway has little effect on the solidification dynamics. When the heat transfer is not diffusion controlled (the tail where much of the surrounding material is near the melting temperature) and $Pé > 1$, latent heat diffuses slowly, and the profile of the latent heat release becomes important.

From the probability density functions presented in Figure 5 and statistics of Table 3, we observed that equilibrium underpredicts the cooling rate and solidification time by 13.9% and 31.5% respectively compared to Scheil. Linear and sigmoidal paths both overpredicted the cooling rate and solidification time with 120.4% and 33.3% respectively for linear, and 289.8% and 39.2% respectively for sigmoidal. These calculations along with Figures 8-10 suggest that model predictions of solidification dynamics can be highly dependent upon the fraction solid-temperature relation used in the modeling of additive manufacturing. As previously mentioned, one purpose for the development of melt pool transport models such as the one used here is to provide temperature data to microstructural evolution models. To this end, to ensure the as-built microstructures predictions are trustworthy representations of reality, we must first make certain that the temperature data is as reliable as possible, and thus, selection of the solidification pathway much be given careful consideration.

4. Conclusion

The present work used a previously established uncertainty quantification framework [14] to analyze the effect solidification pathway selection has on melt pool geometry and solidification dynamics. Additionally, we examined the assumption that due to insufficient spatial resolution, the latent heat release profiles of the various solidification paths cannot be resolved, and therefore the selection of the solidification pathway is not critical to the reliability of the model. Four solidification pathways reported in the literature were studied, specifically Scheil, equilibrium, linear, and sigmoidal profiles.

Results show the melt pool width and depth predictions are insensitive to the solidification pathway (save equilibrium due to the difference in freezing range) used as the spatial resolution through these regions of the melt pool is too coarse to differentiate between the latent heat release profiles. As such, the authors conclude that if melt pool width and depth (useful for scan strategy development) are the only outputs of interest, the assumption holds, and any solidification pathway may be used without significant lose in model reliability.

Melt pool length and solidification dynamics were found to be highly sensitive to the pathway selection depending on location within the melt pool. Taking Scheil as the best physical representation, sigmoidal and linear were found to overpredict cooling rates at the liquidus isotherm and overpredict solidification time and mushy zone thickness. This is the result of their

non-physical latent heat evolution profiles which release heat steadily throughout the mushy zone. Equilibrium does show good agreement with the cooling rate at the liquidus isotherm, but the narrow freezing range causes an underprediction in solidification time, mushy zone thickness, and melt pool dimensions. As such, to ensure reliable predictions of solidification dynamics for transport models of the laser powder bed fusion process, careful consideration must be afforded to the selection of solidification pathway.

Acknowledgements

This manuscript has been authored by UT-Battelle, LLC under Contract No. DE-AC05-00OR22725 with the U.S. Department of Energy. The United States Government retains and the publisher, by accepting the article for publication, acknowledges that the United States Government retains a non-exclusive, paid-up, irrevocable, world-wide license to publish or reproduce the published form of this manuscript, or allow others to do so, for United States Government purposes. The Department of Energy will provide public access to these results of federally sponsored research in accordance with the DOE Public Access Plan (http://energy.gov/downloads/doe-public-access-plan).

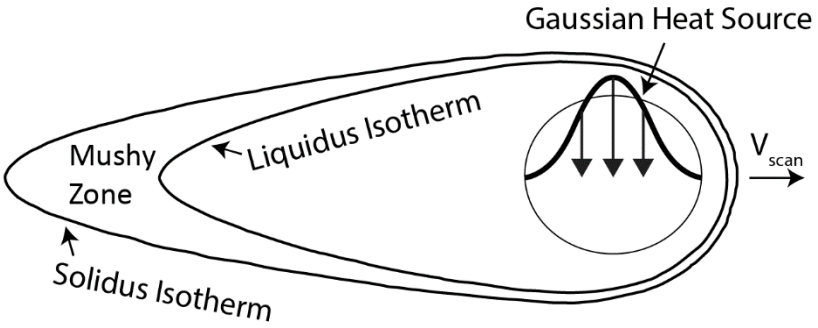

401
402 **Figure 1.** Illustration of melt pool surface with solidus and liquidus isotherms indicated. The
403 mushy zone between these temperatures is where the evolution of latent heat occurs, the profile
404 of which is dictated by the choice in solidification pathway.

405

406

407

408

409

410

411

412

413

414

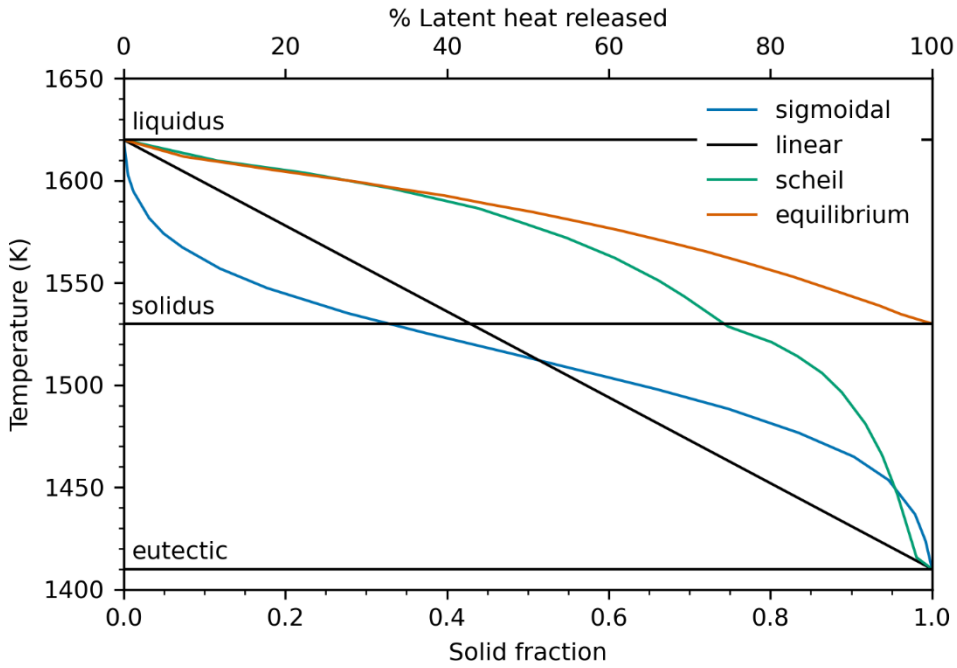

Figure 2. Solid fraction-temperature relations for IN625. Compared to equilibrium, the linear, sigmoidal, and Scheil paths predict a larger freezing range, all three ending at a eutectic temperature.

Table 1. Mean values and measurement method for each input (where applicable), and the associated uncertainty for model inputs.

Parameter	Units	Mean Values	Uncertainty (± 2σ)	Measurement Method
ρ_S	kg/m^3	7670.0	3.33 kg/m^3	Dilatometry
ρ_L	kg/m^3	7670.0	3.33 kg/m^3	Dilatometry
Cp_S	J/kg K	579.28	2.67 %	Calorimetry
Cp_L	J/kg K	750.65	2.67 %	Calorimetry
k_S	W/m K	$8.275 + 0.01472T$	3.33 %	Flash Diffusivity
k_L	W/m K	$4.889 + 0.014743T$	3.33 %	Flash Diffusivity
L_f	J/kg	217,500	2.67 %	Calorimetry
P	W	195	1.67 %	---
V_{scan}	m/s	0.80	2.5 %	----
η	---	0.30	10 %	---

*(S), (L) correspond to solid and liquid IN625

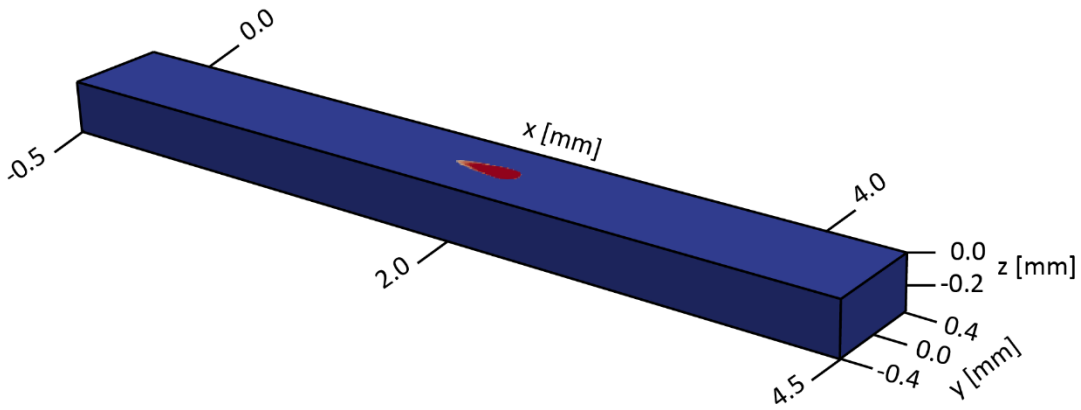

Figure 3. Illustration of the computational domain for the single-line scan. Scan path begins at x = 0.0 and proceeds to x = 4.0. Axes given in mm.

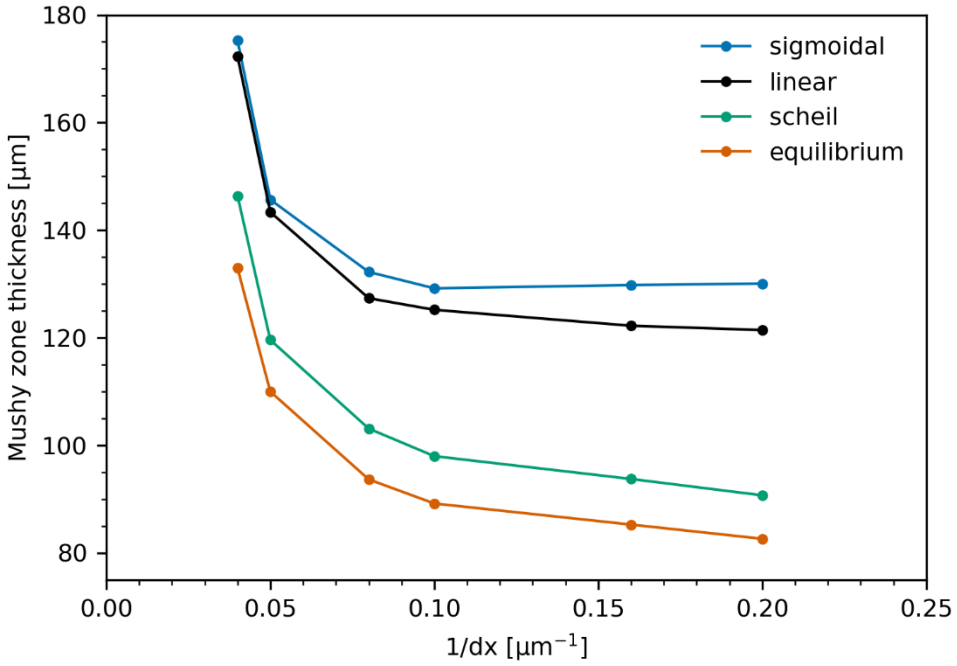

Figure 4. Grid convergence study for mushy zone thickness showing a converged solution is not fully reached even at very fine grid spacings.

476 **Table 2.** Baseline model predictions assuming no uncertainty in input parameters.

	Scheil	**Equilibrium**	**Linear**	**Sigmoidal**
Width [µm]	140.91	134.01	140.35	140.42
Depth [µm]	46.21	42.48	45.84	45.93
Length [µm]	404.91	370.85	418.22	417.91
Cooling rate [K/s]	418,751	360,329	923,000	1,632,218
Surface t_s [µs]	113.77	77.92	151.70	162.37
Mushy zone thickness [µm]	91.0	62.3	121.4	129.9

477

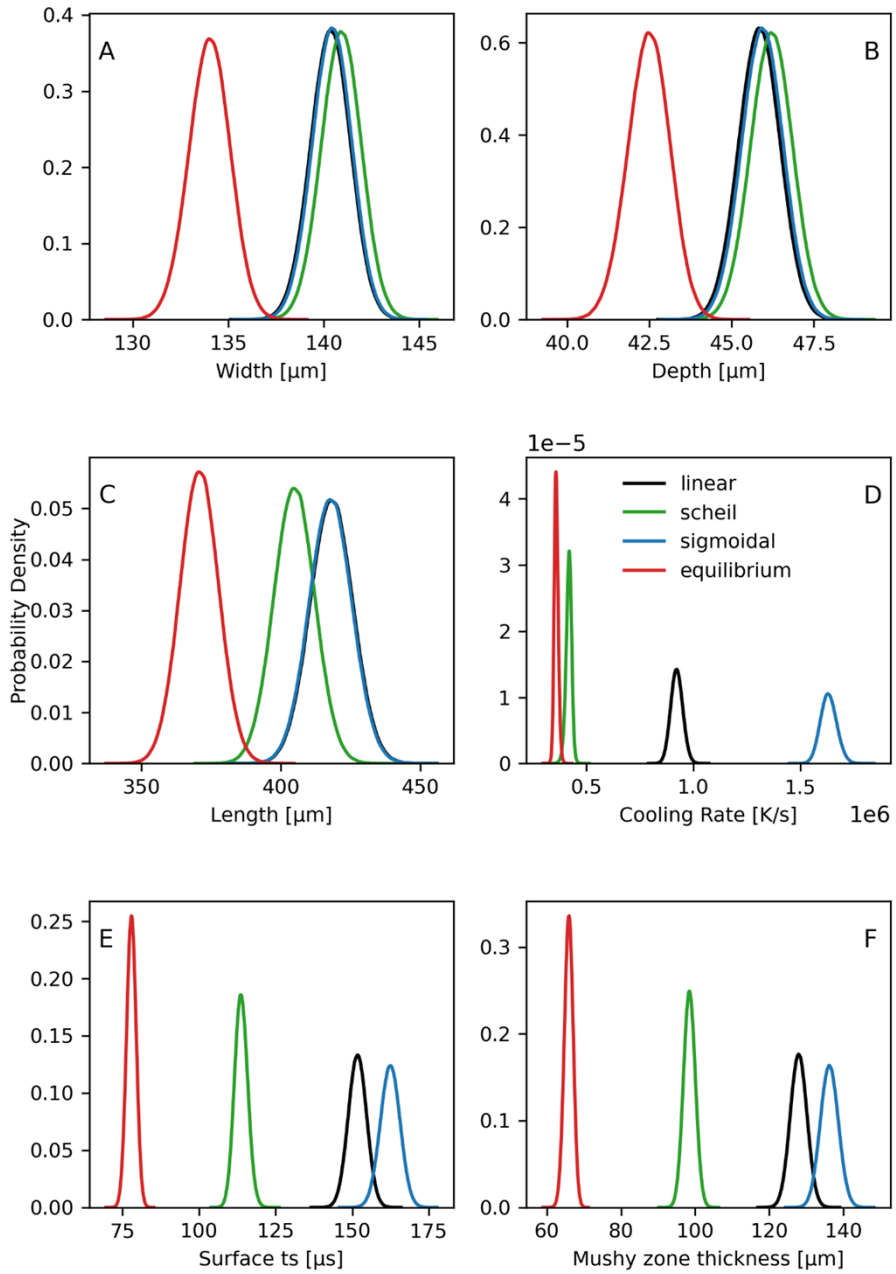

Figure 5. Comparison of probability density functions for each of the solidification pathways. Equilibrium is shown to underpredict all OOI compared to Scheil. Linear and sigmoidal overpredict everything except the melt pool width and depth.

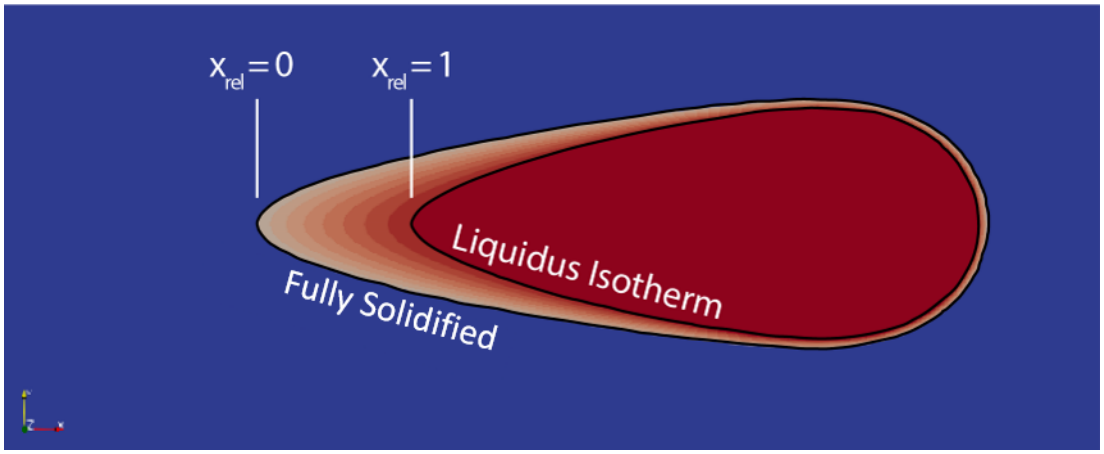

Figure 6. Relative position through the mushy zone allows for direct comparisons between solidification path models despite differences in mushy zone thickness.

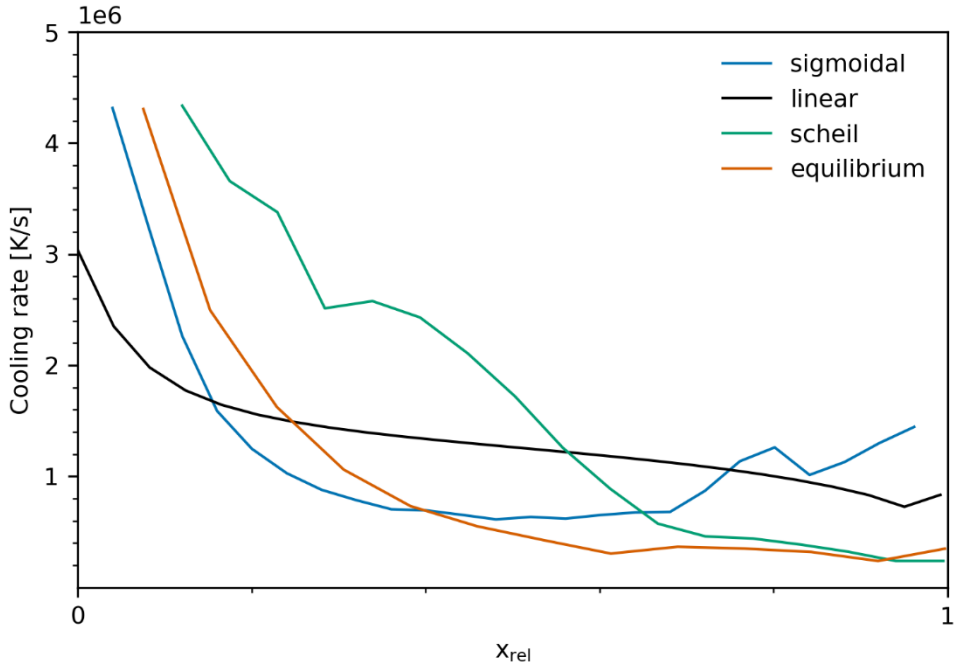

Figure 7. Cooling rate as a function of relative position through the mushy zone where $x_{rel} = 0$ corresponds with the solidus, and $x_{rel} = 1$ the liquidus isotherms. Data was measure at cell centers avoiding cells the isotherm passes through to avoid cells only partially within the mushy zone.

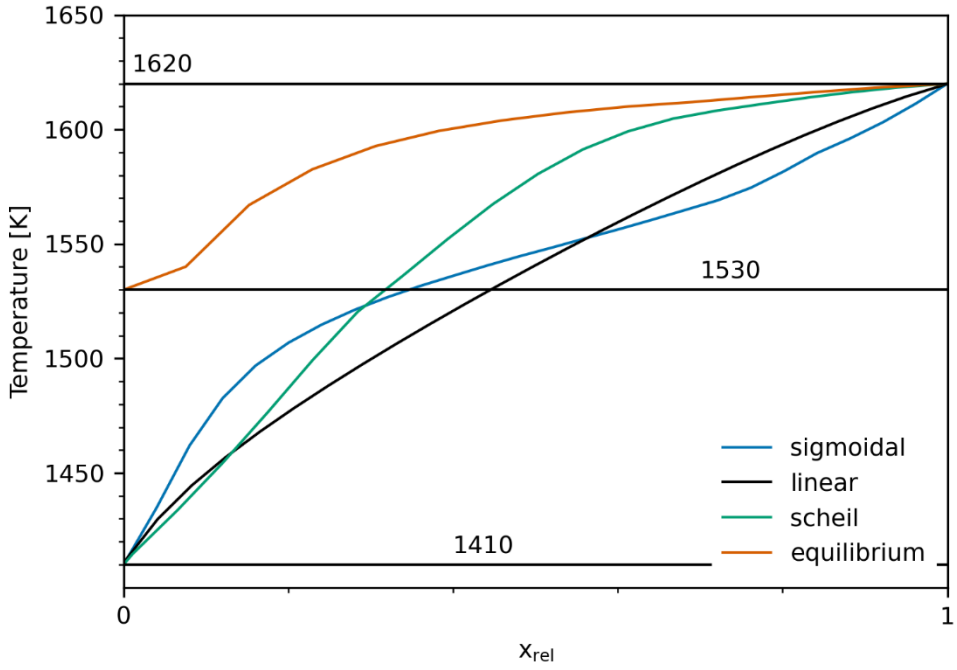

Figure 8. Temperature profile as a function of relative position. The low cooling rates of Scheil and equilibrium produces gradual temperature decreases early on during solidification (right side) but increase later. Sigmoidal and linear solidification curves do not capture these effects.

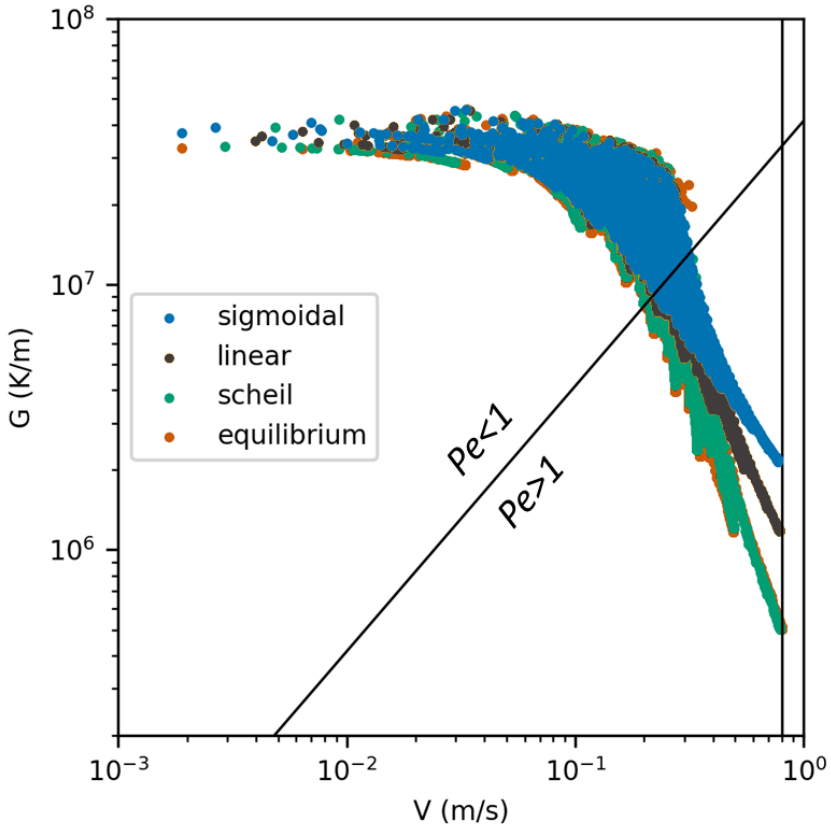

507

508 **Figure 9.** Thermal gradient vs. solidification front velocity for the four different solidification
509 pathways. Sigmoidal and linear show a narrower range (fewer orders of magnitudet) in G values
510 due to their more uniform release of latent heat. Overlay indicates significant dependence on
511 pathway selection when Pé > 1.

512 ## Appendix: Sensitivity Analysis and Sampling Data

513 Following the sensitivity analysis procedure of [14] for each of the solidification pathways
514 used in this work, Figure 10 was created. Comparing the results, it was found the general trends
515 observed in [14] were still present here, and the sensitivity to the aleatoric input parameter
516 uncertainties shown appear independent of the solidification pathway. An exception being the
517 equilibrium curve which appears much lower for the melt pool width, however, this can be
518 explained by the reduced freezing range.

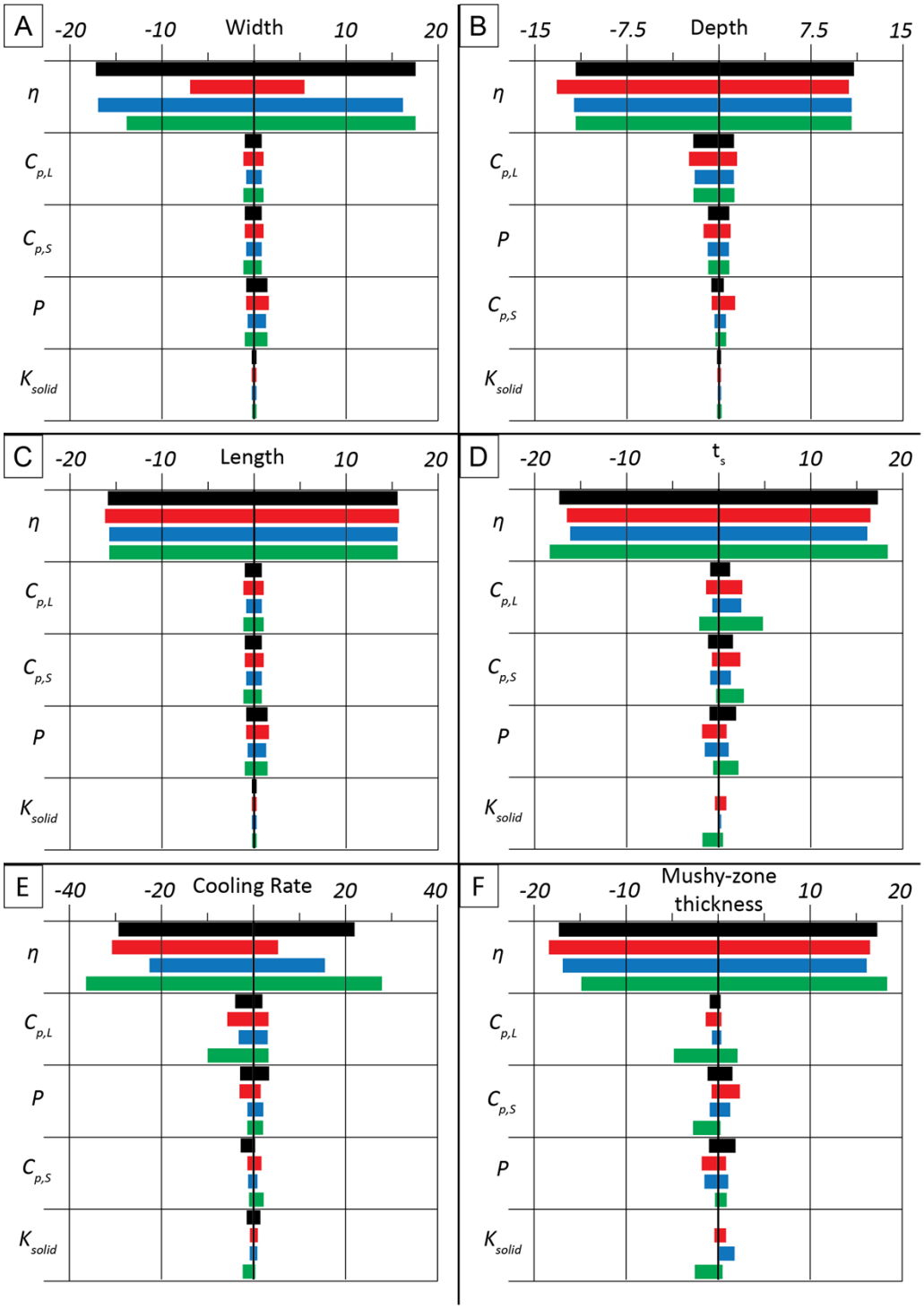

519

520 **Figure 10:** Sensitivity of melt pool dimensions and solidification characteristics for systematic
521 variation in input parameters for the linear (black), sigmoidal (blue), equilibrium (red), and
522 Scheil (green). Prediction uncertainty is predominantly the result of uncertainty in laser
523 absorption (η), solid $(C_{p,s})$ and liquid specific heat capacities $(C_{p,l})$.

524

The next step in the uncertainty analysis is constructing the surrogate models and sampling them 10-million times to generate a large volume of statistical data. The same procedure reported in [14] was followed here for each of the solidification pathways to generate the data presented in Table 3. From this data it is clear the aleatoric uncertainty (best described by the '% of Mean' column, is independent of the solidification pathway selection. It is important to note that while the uncertainty is unaffected, the actual model predictions (best described by the 'Mean' column) are dependent on the pathway.

Table 3. Statistics for the probability density functions generated from the Monte Carlo sampling of the polynomial surrogate models.

Output	Solidification pathway	Mean	2σ	% of Mean
Width [µm]	Scheil	140.91	2.10	1.49
	Equilibrium	134.01	2.15	1.60
	Linear	140.35	2.10	1.50
	Sigmoidal	140.42	2.08	1.48
Depth [µm]	Scheil	46.21	1.28	2.77
	Equilibrium	42.48	1.28	3.01
	Linear	45.84	1.26	2.75
	Sigmoidal	45.93	1.26	2.74
Length [µm]	Scheil	404.91	14.72	3.64
	Equilibrium	370.85	13.86	3.74
	Linear	418.22	15.38	3.68
	Sigmoidal	417.91	15.34	3.67
Cooling rate [K/s]	Scheil	418,751	27,015	6.45
	Equilibrium	360,329	19,112	5.30
	Linear	923,000	56,035	6.07
	Sigmoidal	1,632,218	76,071	4.66
Surface t_s [µs]	Scheil	113.77	4.30	3.78
	Equilibrium	77.92	3.12	4.00
	Linear	151.70	5.96	3.93
	Sigmoidal	162.37	6.41	3.95
Mushy-zone thickness [µm]	Scheil	98.45	3.20	3.25
	Equilibrium	65.90	2.38	3.61
	Linear	127.90	4.50	3.52
	Sigmoidal	136.19	4.88	3.58

References

1. T. DebRoy, H.L. Wei, J.S. Zuback, T. Mukherjee, J.W. Elmer, J.O. Milewski, A.M. Beese, A. Wilson-Heid, A. De, and W. Zhang: *Prog. Mater. Sci.*, 2018, vol. 92, pp. 112-224.
2. R. Liu, Z. Wang, T. Sparks, F. Liou, and J. Newkirk: Laser Additive Manufacturing, M. Brandt, ed., *Woodhead Publishing*, 2017, pp. 351-371.
3. I. Yadroitsev and I. Smurov: *Phys. Procedia*, 2011, vol. 12, pp. 264-270.
4. W.E. King, H.D. Barth, V.M. Castillo, G.F. Gallegos, J.W. Gibbs, D.E. Hahn, C. Kamath, and A.M. Rubenchik: *J. Mater. Proc. Tech.*, 2014, vol. 214, pp. 2915-2925.
5. A.A. Martin, N.P. Calta, S.A. Khairallah, J. Wang, P.J. Depond, A.Y. Fong, V. Thampy, G.M. Guss, A.M. Kiss, K.H. Stone, C.J. Tassone, J. Nelson Weker, M.F. Toney, T. van Buuren, and M.J. Matthews: *Nat. Comm.*, 2019, vol. 10.
6. H.L. Wei, T. Mukherjee, W. Zhang, J.S. Zuback, G.L. Knapp, A. De, and T. DebRoy: *Prog. Mater. Sci.,* 2021, vol. 116.
7. M. S. Mohebbi, V. Ploshikhin: *Add. Manu.*, 2020, vol. 36, art. No. 101726.
8. O. Zinovieva, A. Zinoviev, V. Ploshikhin: *Comput. Mater. Sci.*, 2018, vol. 141, pp. 207-220.
9. M. Rolchigo, R. Carson, J. Belak: *Metals*, 2022, vol. 12, p. 324.
10. L. X. Lu, N. Sridhar, Y. W. Zhang: *Acta Materialia*, 2018, vol. 144, pp. 801-809.
11. X. Gong, K. Chou: *JOM*, 2015, vol. 67, pp. 1176-1182.
12. S. Sahoo, K. Chou: *Add. Manu.*, 2016, vol. 9, pp. 14-24.
13. T. Moges, G. Ameta, and P. Witherell: *J. Manu. Sci. Eng.*, 2019, vol. 141.
14. S. Wells, A. Plotkowski, and M.J.M. Krane: *Met. Mater. Trans. B*, 2021.
15. P.A. Hooper: *Add. Manu.*, 2018, vol. 22, pp. 548-59.
16. W. Zhang, C.H. Kim, and T. DebRoy: *J. App. Phys.*, 2004, vol. 95.
17. W. Yan, W. Ge, Y. Qian, S. Lin, B. Zhou, W.K. Liu, F. Lin, and G.J. Wagner: *Acta Mater*, 2017, vol 134, pp. 324-333.
18. Z.S. Saldi, A. Kidess, S. Kenjereš, C. Zhao, I.M. Richardson, and C.R. Kleijn: *Int. J. Heat and Mass Transf.*, 2013, vol. 66, pp. 879-888.
19. F. Rösler and D. Brüggemann: *Heat and Mass Transf./Waerme- und Stoffuebertragung*, 2011, vol. 47, pp. 1027-33.

20. J. Coleman, A. Plotkowski, B. Stump, N. Raghavan, A.S. Sabau, M.J.M. Krane, J. Heigel, R.E. Ricker, L. Levine, and S.S. Babu: *J. of Heat Transf.,* 2020, vol. 142.
21. M. Stoyanov and C.G. Webster: in *Comput. Math. with Appl.*, 2016, vol. 71, pp. 2449-2465.
22. M. Stoyanov: in *Lecture Notes in Comput. Sci. and Eng.*, 2018, vol. 123, pp. 175-199.
23. Z. Morrow and M. Stoyanov: *SIAM J. on Sci. Comput.*, 2020, vol. 42(4), A2436-A2460.
24. M. Stoyanov: *User Manual: TASMANIAN Sparse Grids*, Oak Ridge National Laboratory, 2015, https://ornl.github.io/TASMANIAN/stable/
25. M. Stoyanov, D. Lebrun-Grandie, J. Burkardt, and D. Munster: TASMANIAN, 2013, https://tasmanian.ornl.gov/index.html
26. J.C. Heigel and B.M. Lane: *J. of Manu. Sci. and Eng.*, 2018, vol. 140, art. No 051012.
27. S. Ghosh, L. Ma, L.E. Levine, R.E. Ricker, M.R. Stoudt, J.C. Heigel, and J.E. Guyer: *JOM*, 2018, vol. 70, pp. 1011-1016.
28. J. Goldak, A. Chakravarti, and M. Bibby: *Met. Mater. Trans. B*, 1984, vol. 15, pp. 299-305.
29. B. Stump, A. Plotkowski and J. Coleman: *Modelling. Simul. Mater. Sci. Eng.*, 2021, vol. 29, art. No. 035001.